



Cite this: *Chem. Sci.*, 2019, 10, 10283 All publication charges for this article have been paid for by the Royal Society of Chemistry

# Synergistic catalysis on Fe–N<sub>x</sub> sites and Fe nanoparticles for efficient synthesis of quinolines and quinazolinones *via* oxidative coupling of amines and aldehydes†

Zhiming Ma,<sup>ab</sup> Tao Song,<sup>\*a</sup> Youzhu Yuan <sup>c</sup> and Yong Yang <sup>\*a</sup>

In this paper, we developed a reusable heterogeneous non-precious iron nanocomposite comprising metallic Fe–Fe<sub>3</sub>C nanoparticles and Fe–N<sub>x</sub> sites on N-doped porous carbon, which allows for highly efficient synthesis of quinolines and quinazolinones *via* oxidative coupling of amines and aldehydes using H<sub>2</sub>O<sub>2</sub> as the oxidant in aqueous solution under mild conditions. A set of quinazolines and quinazolinones were synthesized in high yields with a broad substrate scope and good tolerance of functional groups. Characterization and control experiments disclose that a synergistic effect between the metallic Fe nanoparticles and built-in Fe–N<sub>x</sub> sites is primarily responsible for the outstanding catalytic performance. Furthermore, the iron nanocomposite could be readily recovered for successive use without appreciable loss in catalytic activity and selectivity. This work provides an expedient and sustainable method to access pharmaceutically relevant N-heterocycles.

Received 14th August 2019  
Accepted 20th September 2019

DOI: 10.1039/c9sc04060a

rsc.li/chemical-science

## Introduction

The development of reusable earth-abundant and inexpensive non-precious metal catalysts for innovative organic synthesis is a key technology for a more sustainable production of fine chemicals, pharmaceuticals and agrochemicals. Conventional nanostructured non-precious metal catalysts prepared by impregnation or immobilization are generally only applicable for organic transformations of structurally simple molecules. To further explore their broad application for more challenging and complex synthetic reactions, great efforts have been devoted to rational design and fabrication of nanostructured non-precious metal catalysts with higher potential over the past few decades. Consequently, a number of effective nanostructured non-precious metal (*e.g.*, Fe,<sup>1</sup> Co,<sup>2</sup> Ni,<sup>3</sup> and Mn<sup>4</sup>) catalysts with unique structures or compositions have been developed *via* pyrolysis of either a mixture of metal complexes and/or carbon support<sup>1c–e,2c,2e,f,3b,e</sup> (or Al<sub>2</sub>O<sub>3</sub> (ref. 1f and 2b) or SiO<sub>2</sub> (ref. 2c and 3f)), or a mixture of metal salts and renewable biomass,<sup>14</sup> or metal-organic frameworks (MOFs).<sup>2g–i</sup> The resulting nanostructured

catalysts have demonstrated excellent catalytic performance for a set of organic reactions, such as reductive amination,<sup>3a,d,e</sup> hydrogenation of nitroarenes,<sup>1a,e,2d,e,3c,f</sup> the synthesis of nitriles,<sup>1g,2f</sup> and oxidation of alcohols<sup>2k,l,4a,c–e</sup> and N-heterocycles.<sup>1d,2m</sup>

Among them, nanostructured Fe catalysts are much more attractive due to the earth-abundant, non-toxic, biocompatible, and environmentally benign characteristics of Fe. Specifically, Fe–nitrogen-coordinated carbon catalysts, named Fe–N–C, have recently emerged as a fascinating catalyst for electrocatalysis, in which Fe–N<sub>x</sub> sites are arguably considered as catalytically active sites.<sup>5</sup> Yet, the exploration of Fe–N–C for organic synthesis is still scarce to date.<sup>1c</sup> Furthermore, recent studies disclosed the presence of Fe–N<sub>x</sub> sites in hybrid nanostructured Fe catalysts which were proposed to be responsible for high catalytic reactivity,<sup>1e</sup> while no clear and solid evidence was observed or intense investigation was done to support such a hypothesis so far. As such, elucidation of the role of Fe–N<sub>x</sub> sites in catalysis is urgently desirable, not only for better understanding the reactions but also for the rational design and preparation of highly active and stable nanostructured Fe–N–C catalysts.

N-heterocycles are ubiquitous in nature and constitute the backbone of numerous natural products, pharmaceutically important molecules, and organic functional materials.<sup>6</sup> Among various N-heterocycles known, quinazolines and quinazolinones are two classes of fused structural motifs with a wide range of pharmacological and biological activities, such as antibacterial, anti-inflammatory, anticonvulsant, antimalarial, antiasthmatic, anti-Alzheimer, and anticancer,<sup>7</sup> and are found in many drugs available on the market (Scheme 1).

<sup>a</sup>Qingdao Institute of Bioenergy and Bioprocess Technology, Chinese Academy of Sciences, Qingdao 266101, P. R. China

<sup>b</sup>University of Chinese Academy of Sciences, Beijing, 100049, P. R. China

<sup>c</sup>State Key Laboratory of Physical Chemistry of Solid Surface, National Engineering Laboratory for Green Chemical Productions of Alcohols-Ethers-Esters, College of Chemistry and Chemical Engineering, Xiamen University, Xiamen 361005, P. R. China

† Electronic supplementary information (ESI) available: Experimental section, supplementary figures and tables, and <sup>1</sup>H/<sup>13</sup>C NMR spectroscopy and HR-MS data for all compounds. See DOI: 10.1039/c9sc04060a



Given the importance of N-heterocycles, a number of synthetic methods have been developed over the past few decades.<sup>8</sup> Despite these significant advances, the most classical and general approaches for the synthesis of quinazolines and quinazolinones still strongly rely on the condensation between *o*-aminobenzylamines and aldehydes followed by the oxidation of the resulting amination intermediates in the laboratory and industry. However, this protocol generally requires the use of a large excess of toxic oxidants, such as DDQ,<sup>9</sup> MnO<sub>2</sub>,<sup>10</sup> PhI(OAc)<sub>2</sub>,<sup>11</sup> and NaClO,<sup>12</sup> or homogeneous transition metal complexes ligated with well-defined ligands,<sup>8d,13</sup> which significantly limit its practical application, especially for pharmaceutical synthesis. Therefore, the development of efficient, stable and cost-effective heterogeneous non-precious metal catalysts for accessing quinazolines and quinazolinones is highly desirable.

In this work, we develop a novel nanostructured iron catalyst derived from pyrolysis of a mixture of iron salt and readily available and renewable N-containing biomass, bamboo shoots, in a facile preparation method. The resultant catalysts comprise mixed phases, including metallic Fe and Fe<sub>3</sub>C nanoparticles (NPs) and Fe–N<sub>x</sub> sites, which exhibited excellent catalytic activity for the oxidative coupling of amines and aldehydes to access N-heterocycles using H<sub>2</sub>O<sub>2</sub> as a green and sustainable oxidant in water under mild conditions. A set of pharmaceutically relevant quinazolines and quinazolinones were synthesized in high yields with a broad substrate scope and good tolerance of functional groups. Further studies reveal that synergistic catalysis on Fe/Fe<sub>3</sub>C NPs and Fe–N<sub>x</sub> sites is primarily responsible for the high efficiency of the reactions. Moreover, the catalyst could be easily recycled several times without significant loss in catalytic activity.

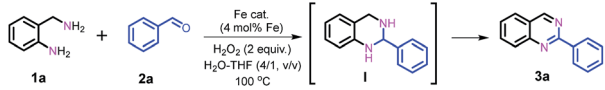
## Results and discussion

Nanostructured iron catalysts were prepared in a facile sequential hydrothermal-pyrolysis process according to a similar procedure as that reported by us.<sup>14</sup> The biochar obtained from hydrothermal treatment of bamboo shoots was homogeneously mixed with Fe(NO<sub>3</sub>)<sub>3</sub> in aqueous solution at 60 °C for 2 h. After evaporation of water, the solid powder was pyrolyzed under a constant nitrogen flow at 800 °C for 2 h (see

details in the ESI†). The as-prepared catalyst was denoted as Fe–Fe<sub>3</sub>C@NC-800. For comparison, Fe–Fe<sub>3</sub>C@NPC-700 and 900 pyrolyzed at 700 and 900 °C were also prepared with the same preparation procedure. The Fe content in the catalysts was determined to be 4.29–4.51 wt% by inductively coupled plasma optical emission spectrometry (ICP-OES) (Table S1†).

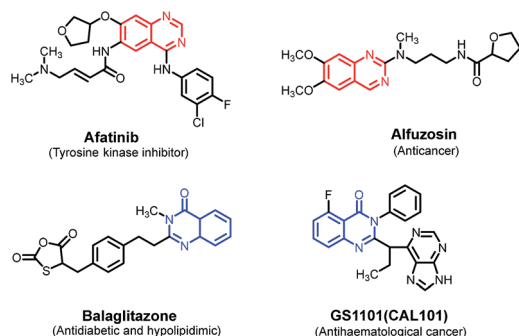
We initiated our studies of the synthesis of quinazolines *via* the oxidative coupling of 2-aminobenzylamine (**1a**) with benzaldehyde (**2a**) as a model reaction using Fe–Fe<sub>3</sub>C@NC-800 as the catalyst to optimize the reaction conditions (Table 1). A set of parameters including the addition amount of benzaldehyde or the oxidant, solvents and reaction temperatures were intensively screened. The reaction was first performed using 1.2 equivalents of benzaldehyde (with respect to **1a**) in the absence of an oxidant in H<sub>2</sub>O at 100 °C. 95% conversion of **1a** was observed, affording 1,2,3,4-tetrahydro-2-phenylquinazoline

Table 1 Optimization of reaction conditions<sup>a</sup>



| Entry           | Catalyst (Fe mol%)                | Solvent              | Conversion <sup>b</sup> (%) | I  | 3a |
|-----------------|-----------------------------------|----------------------|-----------------------------|----|----|
| 1 <sup>c</sup>  | Fe–Fe <sub>3</sub> C@NC-800       | H <sub>2</sub> O     | 95                          | 88 | 7  |
| 2               | Fe–Fe <sub>3</sub> C@NC-800       | H <sub>2</sub> O     | 96                          | 18 | 78 |
| 3 <sup>d</sup>  | Fe–Fe <sub>3</sub> C@NC-800       | H <sub>2</sub> O     | 83                          | 44 | 39 |
| 4 <sup>e</sup>  | Fe–Fe <sub>3</sub> C@NC-800       | H <sub>2</sub> O     | 71                          | 36 | 35 |
| 5               | Fe–Fe <sub>3</sub> C@NC-800       | H <sub>2</sub> O–THF | 100                         | 5  | 95 |
| 6 <sup>f</sup>  | Fe–Fe <sub>3</sub> C@NC-800       | H <sub>2</sub> O–THF | 83                          | 20 | 63 |
| 7               | Fe–Fe <sub>3</sub> C@NC-700       | H <sub>2</sub> O–THF | 88                          | 12 | 76 |
| 8               | Fe–Fe <sub>3</sub> C@NC-900       | H <sub>2</sub> O–THF | 90                          | 6  | 84 |
| 9               | Fe <sub>2</sub> O <sub>3</sub>    | H <sub>2</sub> O–THF | 18                          | 6  | 12 |
| 10              | Fe <sub>3</sub> O <sub>4</sub>    | H <sub>2</sub> O–THF | 29                          | 3  | 26 |
| 11              | Fe(NO <sub>3</sub> ) <sub>3</sub> | H <sub>2</sub> O–THF | 46                          | 3  | 43 |
| 12              | Nano Fe                           | H <sub>2</sub> O–THF | 34                          | 2  | 32 |
| 13              | Fe(II)Pc                          | H <sub>2</sub> O–THF | 89                          | 40 | 49 |
| 14 <sup>g</sup> | —                                 | H <sub>2</sub> O–THF | 15                          | 12 | 3  |

<sup>a</sup> Reaction conditions: 2-aminobenzylamine (**1a**) (0.2 mmol), benzaldehyde (**2a**) (0.24 mmol), catalyst (4 mol% of Fe), H<sub>2</sub>O<sub>2</sub> (2 equivalents with respect to **1a**, 30 wt% in H<sub>2</sub>O), H<sub>2</sub>O (5 mL) or H<sub>2</sub>O–THF (5 mL, 4/1, v/v), 100 °C, 12 h. <sup>b</sup> Determined by GC and GC-MS using 1,3,5-trimethyl-benzene as an internal standard sample and confirmed with their corresponding authentic samples. <sup>c</sup> In the absence of an oxidant. <sup>d</sup> 80 °C. <sup>e</sup> 60 °C. <sup>f</sup> Fe–Fe<sub>3</sub>C@NC-800 (2 mol% of Fe). <sup>g</sup> In the absence of a catalyst.



Scheme 1 Selected examples of market available drugs with quinolone and quinazolinone skeletons.



intermediate (**I**) as the major product with only 7% GC yield of the desired 2-phenylquinazoline **3a** (entry 1). To our delight, 78% GC yield of **3a** was obtained when 2.0 equivalents of  $\text{H}_2\text{O}_2$  as the oxidant were used under otherwise identical conditions (entry 2). A further increase of the amount of  $\text{H}_2\text{O}_2$  resulted in a gradual decrease in the yield of the desired **3a** (Table S2†). 1.2 equivalents of benzaldehyde was found to be the most appropriate ratio for the synthesis of **3a** in terms of catalytic activity and selectivity (Table S3†). A decrease of either the loading of the catalyst  $\text{Fe}-\text{Fe}_3\text{C}@-\text{NC}-800$  or reaction temperature led to a lower yield of **3a** (entries 3, 4, and 6). Further studies show that a mixture  $\text{H}_2\text{O}-\text{THF}$  (v/v, 4/1) as the solvent could pronouncedly improve the catalytic efficiency, and the yield of **3a** could reach as high as 95% under otherwise identical conditions (entry 5 and Table S4†). For comparison, the catalysts  $\text{Fe}-\text{Fe}_3\text{C}@-\text{NC}-700$  and  $\text{Fe}-\text{Fe}_3\text{C}@-\text{NC}-900$  were employed for the reaction, and both showed a relatively lower activity (entries 7 and 8). In addition, control experiments employing commercially available  $\text{Fe}_2\text{O}_3$ ,  $\text{Fe}_3\text{O}_4$ ,  $\text{Fe}(\text{NO}_3)_3$ , iron phthalocyanine ( $\text{Fe}(\text{II})\text{Pc}$ ), and nano Fe powder as catalysts for the reaction show that all exhibited inferior reactivity (entries 9–13). However, in the absence of the catalyst, the reaction took place sluggishly to produce intermediate **I** as the major product (entry 14). These observations clearly indicate that the combination of the catalyst  $\text{Fe}-$

$\text{Fe}_3\text{C}@-\text{NC}-800$  and  $\text{H}_2\text{O}_2$  as the oxidant is essential for the successful synthesis of 2-phenylquinazoline in high yield.

Given such impressive findings, we next investigated the structural properties of the catalyst  $\text{Fe}-\text{Fe}_3\text{C}@-\text{NC}-800$  by means of comprehensive technical skills. The transmission electron microscope image (Fig. 1A) shows that nanoparticles with an average size of 14 nm are homogeneously dispersed on carbon. High resolution TEM images (Fig. 1B and C) further reveal that mixed metallic Fe and  $\text{Fe}_3\text{C}$  NPs as the core were covered with a few layers of a graphitic carbon shell as shown in Fig. 1E. The well-resolved lattice spacing of 0.204, 0.238, and 0.338 nm is consistent with the Fe (110),  $\text{Fe}_3\text{C}$  (210), and graphitic C (002) planes, respectively. High-angle annular dark-field scanning transmission electron microscopy (HAADF-STEM) images (Fig. 1D) demonstrate the homogeneous distribution of Fe, N, O and C atoms over the entire sample. The X-ray diffraction (XRD) pattern (Fig. 1F) discloses the formation of crystalline phases of metallic Fe and  $\text{Fe}_3\text{C}$  with the appearance of characteristic diffraction peaks at  $44.7^\circ$  and  $65^\circ$  and at  $37.6^\circ$ ,  $37.7^\circ$ ,  $39.8^\circ$ ,  $40.6^\circ$ ,  $42.9^\circ$ ,  $43.7^\circ$ ,  $44.9^\circ$ ,  $45.9^\circ$  and  $49.1^\circ$ , corresponding to the (110) and (200) phases of cubic metallic Fe (JCPDS no. 06-0696) and the (121), (210), (002), (201), (211), (102), (220), (031), (112), (221) planes of  $\text{Fe}_3\text{C}$  (cementite, JCPDS no. 35-0772), respectively. Besides, a broad bump peak at  $26.1^\circ$  together with a tiny peak at  $43.1^\circ$  indicates the formation of graphitic carbon upon

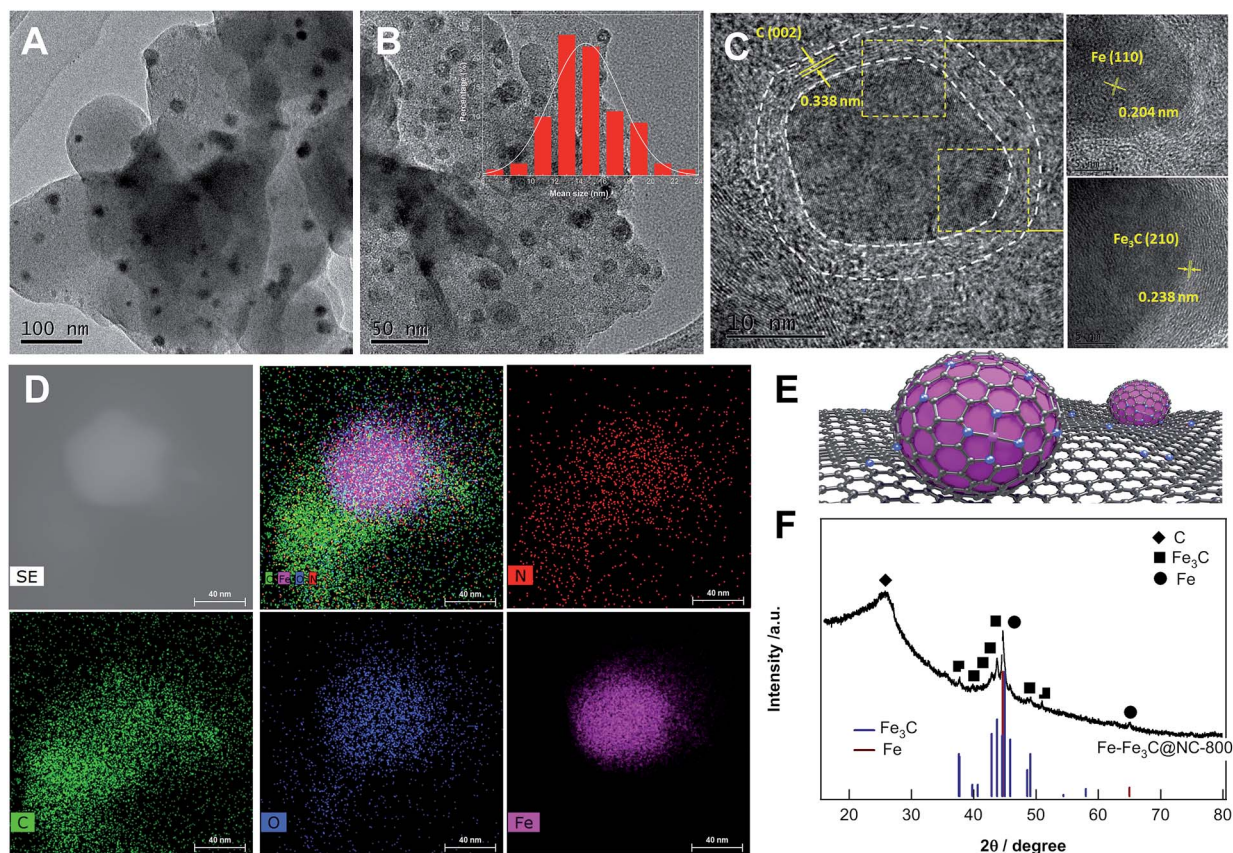


Fig. 1 (A) TEM and (B and C) HR-TEM images of the catalyst  $\text{Fe}-\text{Fe}_3\text{C}@-\text{NC}-800$ ; the inset shows the size distribution of metallic Fe nanoparticles. (D) HAADF-STEM and the corresponding EDX elemental mappings of individual  $\text{Fe}-\text{Fe}_3\text{C}@-\text{NC}-800$ , (E) schematic illustration of the catalyst  $\text{Fe}-\text{Fe}_3\text{C}@-\text{NC}-800$ , and (F) XRD pattern of the catalyst  $\text{Fe}-\text{Fe}_3\text{C}@-\text{NC}-800$ .



pyrolysis at 800 °C. These observations are in good agreement with HR-TEM results. The Raman spectrum (Fig. S2†) provided solid evidence for the formation of graphitic carbon with certain graphitization and defect sites. N<sub>2</sub> adsorption/desorption measurements (Fig. S3†) demonstrate that the catalyst Fe-Fe<sub>3</sub>C@NC-800 possess hierarchically micro-, meso-, and macropores with a high specific surface area and large pore volume (Table S1†).

The N 1s XPS spectrum (Fig. 2A) shows 4 deconvoluted peaks at 398.2, 399.6, 400.4, and 401.3 eV, which are assignable to pyridinic, Fe-N<sub>x</sub>, pyrrolic, and quaternary N, respectively.<sup>5f,14c,d</sup> The Fe 2p XPS spectrum (Fig. 2B) shows 3 peaks, and the peak at 706.8 eV in the Fe 2p<sub>3/2</sub> spectrum can be attributed to zero-valence Fe (metallic iron or carbide), while the peak at 710.4 eV can be assigned to Fe in the Fe(II)-N<sub>x</sub> configuration.<sup>5c-e</sup> Compared with Fe(II)Pc, 0.9 eV shift to a higher value was observed, implying the interaction of Fe-N<sub>x</sub> and metallic Fe NPs.<sup>5h,15</sup> To further investigate the local iron structure of the catalyst Fe-Fe<sub>3</sub>C@NC-800, X-ray absorption spectroscopy (XAS) was performed. The spectroscopy of Fe K-edge X-ray absorption near edge structure (XANES) reveals that the catalyst Fe-Fe<sub>3</sub>C@NC-800 almost overlaps with that of Fe(II)Pc, indicating the possible remaining Fe-N<sub>4</sub> structure (Fig. 2C), which is further confirmed from the Fe K-edge extended X-ray absorption fine structure (EXAFS) in Fig. 2D. From the shape and amplitude of the first strong peak at ≈ 1.5 Å, it is clear that the bonding environment in the first shell of the catalyst Fe-Fe<sub>3</sub>C@NC-800 is notably similar to that of Fe(II)Pc, suggesting that it more likely contains FeN<sub>4</sub> complex structures.<sup>5h,16</sup> Besides, the peaks at ≈ 2.1 Å, assignable to Fe-Fe interactions, reveals the presence of an iron-based crystalline structure in the catalyst Fe-Fe<sub>3</sub>C@NC-800.

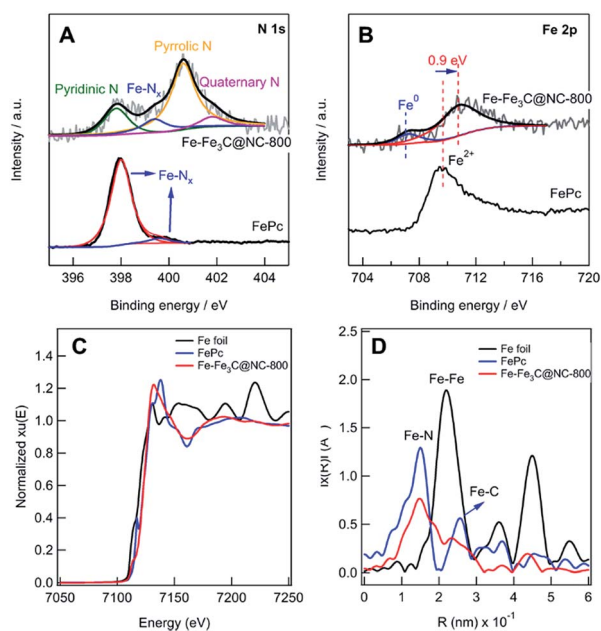


Fig. 2 (A) The deconvoluted N 1s and (B) Fe 2p spectra of FePc and the catalyst Fe-Fe<sub>3</sub>C@NC-800. (C) XANES spectra and (D) Fourier transform (FT) of the Fe K-edge EXAFS data of the catalyst Fe-Fe<sub>3</sub>C@NC-800, Fe foil and FePc.

Taking all characterization results into account, we can conclude that the as-prepared catalyst Fe-Fe<sub>3</sub>C@NC-800 comprises core-shell structured nanoparticles with metallic Fe and Fe<sub>3</sub>C NPs as the core and layers of graphitic carbon as the shell and coordinated Fe-N<sub>x</sub> sites as well. To unveil the catalytically active sites for the oxidative coupling reaction, a set of control experiments were carried out. First, the catalyst Fe-Fe<sub>3</sub>C@NC-800 was leached with acid to remove the metallic Fe NPs, denoted as Fe-N<sub>x</sub>@NC-800 (see details in the ESI†). The HRTEM images and XRD pattern of the acid-etched catalyst Fe-N<sub>x</sub>@NC-800 (Fig. S7 and S8†) show that no nanoparticles were found with preserved hollow-centered graphitic carbon layers. Such a finding further verifies the core-shell structure of the catalyst Fe-Fe<sub>3</sub>C@NC-800. When the acid-etched catalyst Fe-N<sub>x</sub>@NC-800 was subjected to the optimized reaction conditions for the benchmark reaction, a remarkable decrease in both conversion of **1a** and yield of **3a** was observed, as shown in Fig. 3. This result indicates that metallic Fe NPs are necessary for the high catalytic activity, especially for the oxidative dehydrogenation to form the aromatized product **3a**. It is known that SCN<sup>-</sup> ions can poison Fe-N<sub>x</sub> sites in catalysis.<sup>1c,5h</sup> Second, the benchmark reaction was performed using the acid-etched catalyst Fe-N<sub>x</sub>@NC-800 with the addition of NaSCN under otherwise identical conditions. In this case, a further decrease in activity was achieved, clearly implying that Fe-N<sub>x</sub> sites indeed boost the reaction. In parallel, Fe(II)Pc is more active for coupling but with lower selectivity to **3a**, while nano Fe powder was just in opposite position (Fig. 3). In addition, the catalytic activity has a good correlation with the content of Fe-N<sub>x</sub> in the catalysts Fe-Fe<sub>3</sub>C@NC-T as shown in Fig. S9,† that is, the higher the content of Fe-N<sub>x</sub>, the better the activity towards the desired product **3a**. As such, these results unambiguously corroborate that metallic Fe and Fe<sub>3</sub>C nanoparticles and coordinated Fe-

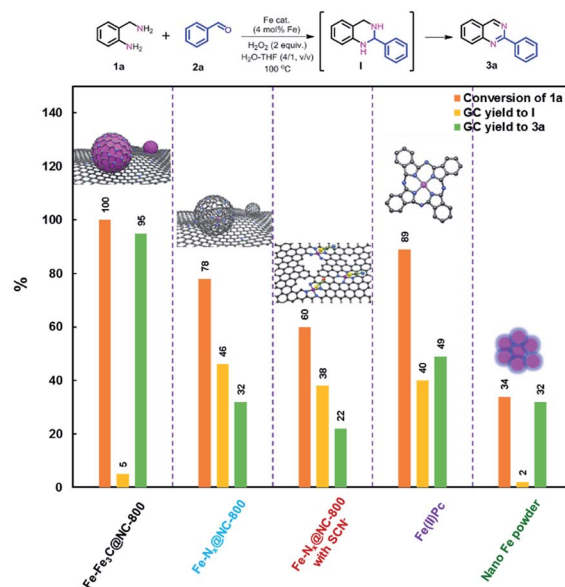


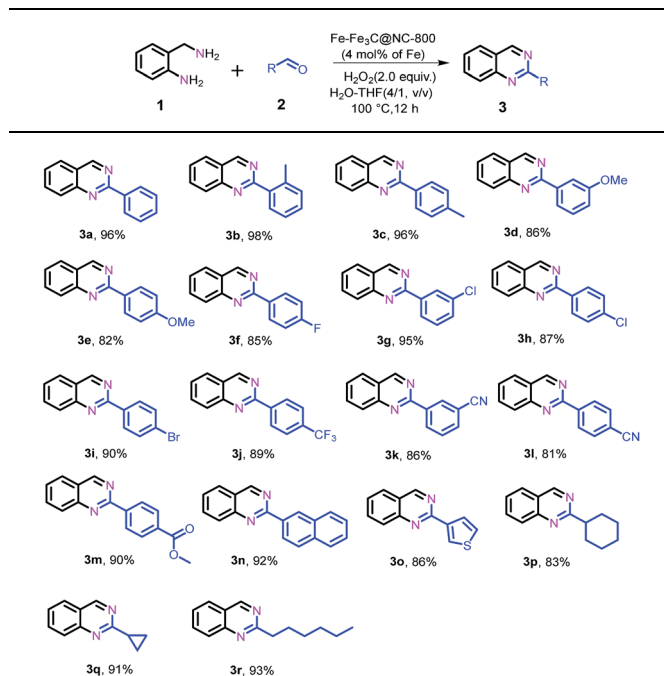
Fig. 3 Comparison of catalytic performance over different catalysts for the benchmark reaction.



$N_x$  in the catalyst  $\text{Fe}-\text{Fe}_3\text{C}@\text{NC}-800$  are synergistically responsible for the coupling reaction to achieve excellent catalytic activity.

Subsequently, further efforts were made to elucidate the individual role of the catalyst  $\text{Fe}-\text{Fe}_3\text{C}@\text{NC}-800$  and the oxidant  $\text{H}_2\text{O}_2$  in this cascade coupling process. As stated above, the combination of the catalyst  $\text{Fe}-\text{Fe}_3\text{C}@\text{NC}-800$  and oxidant  $\text{H}_2\text{O}_2$  is a prerequisite for the success of the coupling to afford the desired quinazoline **3a**, which was reinforced by the control experiments as shown in Scheme 2. In the absence of either the catalyst or oxidant, trace amounts of **3a** were achieved with the formation of intermediate **I** being the major product instead (Scheme 2, entries 2 and 4). Particularly, the coupling underwent sluggishly in the absence of  $\text{H}_2\text{O}_2$ , and only 15% of **1a** was converted. This observation clearly indicates the critical role of the catalyst  $\text{Fe}-\text{Fe}_3\text{C}@\text{NC}-800$  to efficiently boost the entire process. Furthermore, when the intermediate **I** was subjected to the standard conditions, quantitative conversion to **3a** was obtained (Scheme 2, entry 5). Once again, however, in the absence of either the catalyst or oxidant, the efficiency of the oxidative dehydrogenation is significantly low, yielding **3a** in 12% and 10% yield, respectively, under otherwise identical conditions (Scheme 2, entries 6 and 7). As such, we can safely conclude that the catalyst  $\text{Fe}-\text{Fe}_3\text{C}@\text{NC}-800$  participates in the condensation and oxidation steps and significantly facilitates the reaction, while the oxidant  $\text{H}_2\text{O}_2$  benefits the dehydrogenation for aromatization to produce N-heterocycles.

After identifying the optimal reaction conditions and the catalytically active sites, we subsequently explored the generality of this protocol for the synthesis of 2-substituted quinazolines. As shown in Table 2, in general, various benzaldehydes bearing electron-donating and -withdrawing groups could efficiently couple with 2-aminobenzylamine (**1a**) to give their corresponding quinazolines in high yields, while benzaldehydes substituted by electron-donating groups (**2b-e**) gave relatively higher yields than those substituted with electron-withdrawing

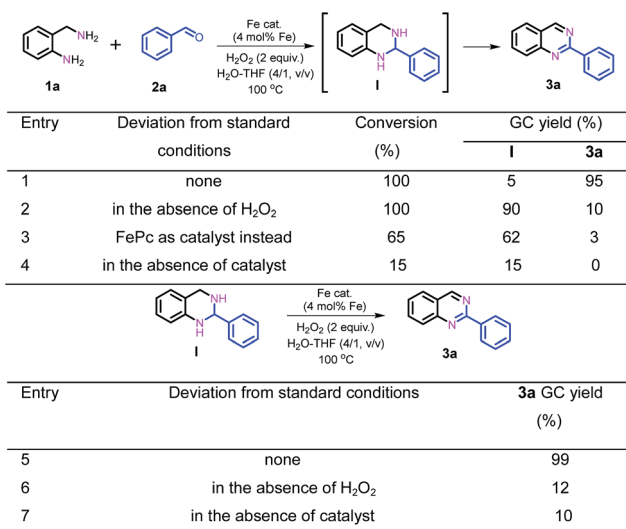
Table 2 Substrate scope for the synthesis of quinazolines<sup>a</sup>

<sup>a</sup> Reaction conditions: 2-aminobenzylamine (**1a**) (0.2 mmol), aldehyde (0.24 mmol),  $\text{Fe}-\text{Fe}_3\text{C}@\text{NC}-800$  (4 mol% of Fe),  $\text{H}_2\text{O}_2$  (2 equivalents with respect to **1a**, 30% in  $\text{H}_2\text{O}$ ),  $\text{H}_2\text{O}-\text{THF}$  (5 mL, 4/1, v/v), 100 °C, 12 h. Yields of isolated product are reported.

groups (**2j-m**). Halogen-substituted benzaldehydes, such as -F, -Cl and -Br, were tolerated under the present conditions, yielding the desired quinazolines (**2f-i**) in 85–95% yields. Heterocyclic aldehydes such as 3-thiophenecarboxaldehyde (**2o**) were also suitable as the coupling partner to deliver their corresponding quinazoline (**2o**) in 86% yield. In addition, aliphatic aldehydes, such as cyclohexanecarboxaldehyde (**2p**), cyclopropanecarboxaldehyde (**2q**) and heptaldehyde (**2r**), could also efficiently couple with **1a** to give the desired quinazolines **3p**, **3q** and **3r** in 83%, 91% and 93% yields, respectively.

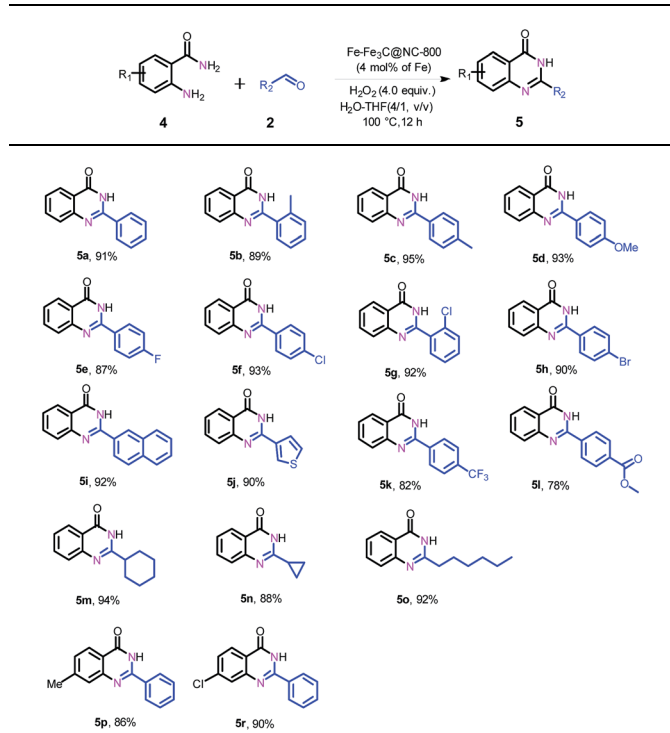
Next, we further explored the substrate scope of the oxidative coupling of 2-aminobenzamide (**4a**) with various aldehydes (**2**) to synthesize quinazolinones under the optimal reaction conditions. To our delight, a broad spectrum of quinazolinones were successfully synthesized in high isolated yields as shown in Table 3. 2-Aminobenzamide could efficiently couple with benzyl aldehydes bearing electron-withdrawing and electron-donating groups as well as halogens. Likewise, heterocyclic and aliphatic aldehydes are also tolerated under the present conditions to deliver their corresponding quinazolinones in high yields. In addition, substituted 2-aminobenzamides are compatible for oxidative coupling too.

Durability/recyclability of a heterogeneous catalyst is critical for sustainable and practical applications. To test the durability of  $\text{Fe}-\text{Fe}_3\text{C}@\text{NC}-800$ , the used catalyst was collected, washed, and dried after completion of an oxidative coupling experiment for the synthesis of 2-phenylquinazoline (**2a**). As shown in Fig. S10,<sup>†</sup> the catalytic activity and selectivity remained high



Scheme 2 Elucidation of the individual role of the catalyst  $\text{Fe}-\text{Fe}_3\text{C}@\text{NC}-800$  and the oxidant  $\text{H}_2\text{O}_2$ .



Table 3 Substrate scope for the synthesis of quinazolinones<sup>a</sup>

<sup>a</sup> Reaction conditions: 2-aminobenzamide (4) (0.2 mmol), aldehyde (0.24 mmol), Fe-Fe<sub>3</sub>C@NC-800 (4 mol% of Fe), H<sub>2</sub>O<sub>2</sub> (4 equivalents with respect to 1a, 30% in H<sub>2</sub>O), H<sub>2</sub>O-THF (5 mL, 4/1, v/v), 100 °C, 12 h. Yields of isolated product are reported.

with negligible changes after six recycles, demonstrating the high durability of this catalyst.

## Conclusion

In conclusion, we developed a reusable heterogeneous earth-abundant iron nanostructured catalyst comprising metallic Fe and Fe<sub>3</sub>C nanoparticles as the core covered by a few layers of N-doped graphitic carbon and coordinated Fe-N<sub>x</sub> sites as well in a facile and cost-effective manner. The resultant best catalyst Fe-Fe<sub>3</sub>C@NC-800 demonstrated excellent catalytic activity for oxidative coupling of amines with aldehydes to access a broad set of quinazolines and quinazolinones. The process was performed in a green and sustainable manner under mild reaction conditions with good tolerance of multifunctional groups. Moreover, the catalyst could be readily recovered for successive reuse without significant loss in activity and selectivity. Synergistic catalysis on Fe-N<sub>x</sub> sites and metallic Fe-Fe<sub>3</sub>C nanoparticles is primarily responsible for the superior activity and stability. This work not only demonstrates the potential of the nanostructured Fe-N-C catalyst for complex synthetic reactions but also provides a new efficient and sustainable method for the synthesis of pharmaceutically important N-heterocycles.

## Conflicts of interest

There are no conflicts to declare.

## Acknowledgements

The authors would like to acknowledge the financial support from the Key Technology R&D Program of Shandong Province (2019GGX102075) and the 13th-Five Key Project of the Chinese Academy of Sciences (Grant No. Y7720519KL). Y. Y also acknowledges the support from the Royal Society (UK) for a Newton Advanced Fellowship (NAF-R2-180695).

## Notes and references

- Selected examples of Fe-based catalysts: (a) R. Yun, S. Zhang, W. Ma, X. Lv, S. Liu, T. Sheng and S. Wang, *Inorg. Chem.*, 2019, **58**, 9469–9475; (b) J. Xie, K. Yin, A. Serov, K. Artyushkova, H. N. Pham, X. Sang, R. R. Unocic, P. Atanassov, A. K. Datye and R. J. Davis, *ChemSusChem*, 2017, **10**, 359–362; (c) W. Liu, L. Zhang, X. Liu, X. Liu, X. Yang, S. Miao, W. Wang, A. Wang and T. Zhang, *J. Am. Chem. Soc.*, 2017, **139**, 10790–10798; (d) X. Cui, Y. Li, S. Bachmann, M. Scalone, A.-E. Surkus, K. Junge, C. Topf and M. Beller, *J. Am. Chem. Soc.*, 2015, **137**, 10652–10658; (e) R. V. Jagadeesh, A.-E. Surkus, H. Junge, M.-M. Pohl, J. Radnik, J. Rabeah, H. Huan, V. Schünemann, A. Brückner and M. Beller, *Science*, 2013, **342**, 1073–1076; (f) J. Li, J. Zhang, S. Wang, G. Xu, H. Wang and D. G. Vlachos, *ACS Catal.*, 2019, **9**, 1564–1577; (g) R. V. Jagadeesh, H. Junge and M. Beller, *ChemSusChem*, 2015, **8**, 92–96.
- Selected examples of Co-based catalysts: (a) G. Li, H. Yang, H. Zhang, Z. Qi, M. Chen, W. Hu, L. Tian, R. Nie and W. Huang, *ACS Catal.*, 2018, **8**, 8396–8405; (b) H. Huang, M. Tan, X. Wang, M. Zhang, S. Guo, X. Zou and X. Lu, *ACS Appl. Mater. Interfaces*, 2018, **10**, 5413–5428; (c) F. Chen, A.-E. Surkus, L. He, M.-M. Pohl, J. Radnik, C. Topf, K. Junge and M. Beller, *J. Am. Chem. Soc.*, 2015, **137**, 11718–11724; (d) Z. Wei, J. Wang, S. Mao, D. Su, H. Jin, Y. Wang, F. Xu, H. Li and Y. Wang, *ACS Catal.*, 2015, **5**, 4783–4789; (e) P. Zhou, L. Jiang, F. Wang, K. Deng, K. Lv and Z. Zhang, *Sci. Adv.*, 2017, **3**, e1601945; (f) F. A. Westerhaus, R. V. Jagadeesh, G. Wienhofer, M.-M. Pohl, J. Radnik, A.-E. Surkus, J. Rabeah, K. Junge, H. Junge, M. Nielsen, A. Bruckner and M. Beller, *Nat. Chem.*, 2013, **5**, 537–543; (g) R. V. Jagadeesh, K. Murugesan, A. S. Alshammari, H. Neumann, M.-M. Pohl, J. Radnik and M. Beller, *Science*, 2017, **358**, 326–332; (h) K. Shen, X. Chen, J. Chen and Y. Li, *ACS Catal.*, 2016, **6**, 5887–5903; (i) X. Ma, Y.-X. Zhou, H. Liu, Y. Li and H.-L. Jiang, *Chem. Commun.*, 2016, **52**, 7719–7722; (j) K. Natte, R. V. Jagadeesh, M. Sharif, H. Neumann and M. Beller, *Org. Biomol. Chem.*, 2016, **14**, 3356–3359; (k) L. Zhang, A. Wang, W. Wang, Y. Huang, X. Liu, S. Miao, J. Liu and T. Zhang, *ACS Catal.*, 2015, **5**, 6563–6572; (l) W. Zhong, H. Liu, C. Bai, S. Liao and Y. Li, *ACS Catal.*, 2015, **5**, 1850–1856; (m) A. V. Iosub and S. S. Stahl, *Org. Lett.*, 2015, **17**, 4404–4407.
- Selected examples of Ni-based catalysts: (a) K. Murugesan, M. Beller and R. V. Jagadeesh, *Angew. Chem., Int. Ed.*, 2019, **58**, 5064–5068; (b) P. Ryabchuk, A. Agapova,



- C. Kreyenschulte, H. Lund, H. Junge, K. Junge and M. Beller, *Chem. Commun.*, 2019, **55**, 4969–4972; (c) F. Yang, M. Wang, W. Liu, B. Yang, Y. Wang, J. Luo, Y. Tang, L. Hou, Y. Li, Z. Li, B. Zhang, W. Yang and Y. Li, *Green Chem.*, 2019, **21**, 704–711; (d) Y. Zhang, H. Yang, Q. Chi and Z. Zhang, *ChemSusChem*, 2019, **12**, 1246–1255; (e) G. Hahn, P. Kunnas, N. de Jonge and R. Kempe, *Nat. Catal.*, 2018, **2**, 71–77; (f) P. Ryabchuk, G. Agostini, M.-M. Pohl, H. Lund, A. Agapova, H. Junge, K. Junge and M. Beller, *Sci. Adv.*, 2018, **4**, eaat0761.
- 4 Selected examples of Mn-based catalysts: (a) J. Fei, L. Sun, C. Zhou, H. Ling, F. Yan, X. Zhong, Y. Lu, J. Shi, J. Huang and Z. Liu, *Nanoscale Res. Lett.*, 2017, **12**, 23; (b) E. Skliri, S. Papadogiorgakis, I. N. Lykakis and G. S. Armatas, *ChemPlusChem*, 2017, **82**, 136–143; (c) K. Dhanalaxmi, R. Singuru, S. K. Kundu, B. M. Reddy, A. Bhaumik and J. Mondal, *RSC Adv.*, 2016, **6**, 36728–36735; (d) J. Mondal, P. Borah, S. Sreejith, K. T. Nguyen, X. Han, X. Ma and Y. Zhao, *ChemCatChem*, 2014, **6**, 3518–3529; (e) H.-Y. Sun, Q. Hua, F.-F. Guo, Z.-Y. Wang and W.-X. Huang, *Adv. Synth. Catal.*, 2012, **354**, 569–573.
- 5 Selected examples of Fe-N-C catalysts: (a) X. Wan, X. Liu, Y. Li, R. Yu, L. Zheng, W. Yan, H. Wang, M. Xu and J. Shui, *Nat. Catal.*, 2019, **2**, 259–268; (b) X. Fu, N. Li, B. Ren, G. Jiang, Y. Liu, F. M. Hassan, D. Su, J. Zhu, L. Yang, Z. Bai, Z. P. Cano, A. Yu and Z. Chen, *Adv. Energy Mater.*, 2019, **9**, 1803737; (c) H. Wang, F.-X. Yin, N. Liu, R.-H. Kou, X.-B. He, C.-J. Sun, B.-H. Chen, D.-J. Liu and H.-Q. Yin, *Adv. Funct. Mater.*, 2019, **29**, 1901531; (d) Y. Mun, S. Lee, K. Kim, S. Kim, S. Lee, J. W. Han and J. Lee, *J. Am. Chem. Soc.*, 2019, **141**, 6254–6262; (e) Q. Wang, Y. Lei, Z. Chen, N. Wu, Y. Wang, B. Wang and Y. Wang, *J. Mater. Chem. A*, 2018, **6**, 516–526; (f) G. Yang, W. Choi, X. Pu and C. Yu, *Energy Environ. Sci.*, 2015, **8**, 1799–1807; (g) Q. Lin, X. Bu, A. Kong, C. Mao, X. Zhao, F. Bu and P. Feng, *J. Am. Chem. Soc.*, 2015, **137**, 2235–2238; (h) W.-J. Jiang, L. Gu, L. Li, Y. Zhang, X. Zhang, L.-J. Zhang, J.-Q. Wang, J.-S. Hu, Z. Wei and L.-J. Wan, *J. Am. Chem. Soc.*, 2016, **138**, 3570–3578; (i) J. Li, S. Ghoshal, W. Liang, M.-T. Sougrati, F. Jaouen, B. Halevi, S. McKinney, G. McCool, C. Ma, X. Yuan, Z.-F. Ma, S. Mukerjee and Q. Jia, *Energy Environ. Sci.*, 2016, **9**, 2418–2432; (j) L. Jiao, G. Wan, R. Zhang, H. Zhou, S.-H. Yu and H.-L. Jiang, *Angew. Chem., Int. Ed.*, 2018, **57**, 8525–8529; (k) L. Jiao and H.-L. Jiang, *Chem*, 2019, **5**, 786–804.
- 6 (a) K. Nepali, H.-Y. Lee and J.-P. Liou, *J. Med. Chem.*, 2019, **62**, 2851–2893; (b) P. D. Leeson and B. Springthorpe, *Nat. Rev. Drug Discovery*, 2007, **6**, 881–890; (c) J. P. Michael, *Nat. Prod. Rep.*, 2008, **25**, 166–187; (d) P. M. S. Bedi, V. Kumar and M. P. Mahajan, *Bioorg. Med. Chem. Lett.*, 2004, **14**, 5211–5213.
- 7 (a) H. Li, L. He, H. Neumann, M. Beller and X.-F. Wu, *Green Chem.*, 2014, **16**, 1336–1343; (b) A. T. Baviskar, C. Madaan, R. Preet, P. Mohapatra, V. Jain, A. Agarwal, S. K. Guchhait, C. N. Kundu, U. C. Banerjee and P. V. Bharatam, *J. Med. Chem.*, 2011, **54**, 5013–5030; (c) G. Marzaro, A. Guiotto and A. Chilin, *Expert Opin. Ther. Pat.*, 2012, **22**, 223–252; (d) J. P. Michael, *Nat. Prod. Rep.*, 2008, **25**, 166–187; (e) D. Sharma, B. Narasimhan, P. Kumar, V. Judge, R. Narang, E. D. Clercq and J. Balzarini, *Eur. J. Med. Chem.*, 2009, **44**, 2347–2353.
- 8 Selected examples for the synthesis of N-heterocycles: (a) Y. Liang, Z. Tan, H. Jiang, Z. Zhu and M. Zhang, *Org. Lett.*, 2019, **21**, 4725–4728; (b) T. Chatterjee, D. I. Kim and E. J. Cho, *J. Org. Chem.*, 2018, **83**, 7423–7430; (c) X. Yu, L. Gao, L. Jia, Y. Yamamoto and M. Bao, *J. Org. Chem.*, 2018, **83**, 10352–10358; (d) S. Parua, R. Sikari, S. Sinha, G. Chakraborty, R. Mondal and N. D. Paul, *J. Org. Chem.*, 2018, **83**, 11154–11166; (e) I. Khan, A. Ibrar, N. Abbas and A. Saeed, *Eur. J. Med. Chem.*, 2014, **76**, 193–244; (f) B. Han, X.-L. Yang, C. Wang, Y.-W. Bai, T.-C. Pan, X. Chen and W. Yu, *J. Org. Chem.*, 2012, **77**, 1136–1142.
- 9 S. Rachakonda, P. S. Pratap and M. V. B. Rao, *Synthesis*, 2012, **44**, 2065–2069.
- 10 Z. Zhang, M. Wang, C. Zhang, Z. Zhang, J. Lu and F. Wang, *Chem. Commun.*, 2015, **51**, 9205–9207.
- 11 M. Saha, P. Mukherjee and A. R. Das, *Tetrahedron Lett.*, 2017, **58**, 2044–2049.
- 12 Y.-Y. Peng, Y. Zeng, G. Qiu, L. Cai and V. W. Pike, *J. Heterocycl. Chem.*, 2010, **47**, 1240–1245.
- 13 A. E. Wendlandt and S. S. Stahl, *J. Am. Chem. Soc.*, 2014, **136**, 506–512.
- 14 (a) T. Song, Z. Ma and Y. Yang, *ChemCatChem*, 2019, **11**, 1313–1319; (b) T. Song, P. Ren, Y. Duan, Z. Wang, X. Chen and Y. Yang, *Green Chem.*, 2018, **20**, 4629–4637; (c) Y. Duan, T. Song, X. Dong and Y. Yang, *Green Chem.*, 2018, **20**, 2821–2828; (d) X. Dong, Z. Wang, Y. Duan and Y. Yang, *Chem. Commun.*, 2018, **54**, 8913–8916.
- 15 Y. Chen, S. Ji, Y. Wang, J. Dong, W. Chen, Z. Li, R. Shen, L. Zheng, Z. Zhuang, D. Wang and Y. Li, *Angew. Chem., Int. Ed.*, 2017, **129**, 1–6.
- 16 (a) G. Wu, K. L. More, C. M. Johnston and P. Zelenay, *Science*, 2011, **332**, 443–447; (b) J. Yang, D.-J. Liu, N. N. Kariuki and L. X. Chen, *Chem. Commun.*, 2008, 329–331.

